Article

In-situ Li$_2$O-atmosphere assisted solvent-free route to produce highly conductive Li$_7$La$_3$Zr$_2$O$_{12}$ solid electrolyte

Jiawen Tang[1], Yongjian Zhou[1], Xiaoyi Li[1], Xiao Huang[1,*], Wei Tang[2], Bingbing Tian[1,*] (iD)

[1]International Collaborative Laboratory of 2D Materials for Optoelectronics Science and Technology of Ministry of Education, Institute of Microscale Optoelectronics, Shenzhen University, Shenzhen 518060, Guangdong, China.
[2]Shaanxi Key Laboratory of Energy Chemical Process Intensification, School of Chemical Engineering and Technology, Xi'an Jiaotong University, Xi'an 710049, Shaanxi, China.

Correspondence to: Dr. Xiao Huang, Institute of Microscale Optoelectronics, Shenzhen University, 3688 Nanhai Road, Nanshan District, Shenzhen 518060, Guangdong, China. E-mail: xiao199198@gmail.com; Prof Bingbing Tian, Institute of Microscale Optoelectronics, Shenzhen University, 3688 Nanhai Road, Nanshan District, Shenzhen 518060, Guangdong, China. E-mail: tianbb2011@szu.edu.cn

Abstract

Solid-state batteries have garnered attention due to their potentiality for increasing energy density and enhanced safety. One of the most promising solid electrolytes is garnet-type Li$_7$La$_3$Zr$_2$O$_{12}$ (LLZO) ceramic electrolyte because of its high conductivity and ease of manufacture in ambient air. The complex gas-liquid-solid sintering mechanism makes it difficult to prepare LLZO with excellent performance and high consistency. In this study, an *in-situ* Li$_2$O-atmosphere assisted solvent-free route is developed for producing the LLZO ceramics. First, the lithium-rich additive Li$_6$Zr$_2$O$_7$ (LiZO) is applied to *in-situ* supply Li$_2$O atmosphere at grain boundaries, where its decomposition products (Li$_2$ZrO$_3$) build the bridge between the grain boundaries. Second, comparisons were studied between the effects of dry and wet routes on the crystallinity, surface contamination, and particle size of calcined powders and sintered ceramics. Third, by analyzing the grain boundary composition and the evolution of ceramic microstructure, the impacts of dry and wet routes and lithium-rich additive LiZO on the ceramic sintering process were studied in detail to elucidate the sintering behavior and mechanism. Lastly, exemplary Nb-doped LLZO pellets with 2 wt% LiZO additives sintered at 1,300 °C × 1 min deliver Li$^+$ conductivities of 8.39 × 10^{-4} S cm^{-1} at 25 °C, relative densities of 96.8%, and ultra-high consistency. It is believed that our route sheds light on preparing high-performance LLZO ceramics for solid-state batteries.

Keywords: Solid-state batteries, Li$_7$La$_3$Zr$_2$O$_{12}$, *in-situ* supply Li$_2$O atmosphere, solvent-free route

INTRODUCTION

With the development of electric vehicles and mobile vehicles in recent years, the need for lithium-ion batteries has increased significantly. Solid-state lithium metal batteries (SSLMBs) based on solid-state electrolytes are strong candidates for next-generation technologies due to their potential high safety and high energy density[1-3]. SSLMBs transcend the capacity limitations of conventional liquid lithium-ion batteries and answer the transportation industry's requirement for increased power and energy density[4,5]. Therefore, the solid-state electrolyte has received extensive research[6,7]; highly ionic conductive solid electrolytes (SEs), including sulfide electrolytes and oxide electrolytes, have been developed by numerous researchers[8-12].

Among these SEs, $Li_7La_3Zr_2O_{12}$ (LLZO) is attractive due to its high room-temperature ion conductivity $\sim 10^{-3}$ S cm^{-1}[13], wide electrochemical window of 0~4.3 V[14], strong interfacial stability against lithium metal[15], and ease of manufacture in ambient atmosphere[16]. Nevertheless, stoichiometry LLZO is the tetragonal phase at room temperature with two to three orders of magnitude lower Li$^+$ conductivity than the cubic phase[17,18]. Element doping, such as Ta^{5+} and Nb^{5+} at the Zr-site[19,20], Al^{3+} and Ga^{3+} at the Li-site[21,22], is used to successfully stabilize the cubic phase structure. However, the lab-scale production craft of LLZO is less reported[23], requiring a reliable method for research. Due to low cost and suitability for atmospheric settings, the solid-state reaction method is employed for the mass manufacture of LLZO powders and ceramics. Typically, a wet-chemistry method is used to mix the precursors and tailor the powder, requiring the use of a solvent such as ethanol (EA) or isopropanol (IPA). Huang *et al.* developed a non-mother-powder method using a MgO crucible for Ta-doped LLZO ceramics[24]. Although production costs have been lowered, issues such as limited preparation speed and low consistency of the manufactured ceramics remain. Previous works investigated the relationship between lithium loss and densification during the sintering process based on the wet milling[13,25] and further developed the wet route to produce Ta-doped LLZO as the practical example[26]. Although ceramics can be successfully prepared delivering relatively good performances, the problem lies in the narrow parameters at each craft step, which requires careful tuning for each batch of production. In another work, we examined the negative effects of IPA solvents on milled particles[27], where lots of $LiOH \cdot H_2O$ and Li_2CO_3 contaminations formed on the surfaces due to the Li$^+$/H$^+$ exchange[28,29]. Other works have investigated the compatibility, reaction properties and proton exchange between the solvent and LLZO[30-32]. Zheng *et al.* developed a solvent-free method to prepare Ta-doped LLZO ceramics that are more stable to water[33,34]. However, there is a lack of research systematically studying the differences between wet and dry routes for the large-scale production.

On the other hand, due to its high sintering temperature (Zr-site- and Li-site-doped LLZO typically exceeds 1,150 and 1,050 °C, respectively), the lithium loss is a serious problem[35,36]. Traditional mother powder [such as $Li_{6.55}La_3Zr_{1.55}Nb_{0.45}O_{12}$ (Nb-LLZO) with Li content excess 15%] was usually adopted to cover the green pellet or to supplement Li_2O atmosphere. The lithium atmosphere from the mother powder enters the green pellets from the exterior to the interior, which will result in slow and uneven sintering. It is essential to identify inexpensive lithium supplement materials and more advanced lithium supplement procedures. Zheng *et al.* have investigated the *in-situ* lithium supplementation method in previous studies[37,38]. However, they employed wet procedure, and the consistency of the as-prepared ceramics was not further investigated. For large-scale batch preparation of LLZO ceramics with high performance and high consistency, it is critical to simplify the experimental procedure as much as possible combining with *in-situ* lithium supplementation strategy.

The goal of this work is to create a large-scale preparation process platform for LLZO SEs that is dependable and repeatable. Due to the low cost of the Nb element, we chose Nb-doped LLZO as a typical material. The Nb-LLZO was prepared without solvent using the conventional solid-state method, and the high-efficiency sintering of a large number of green pellets was achieved by the "pellet-on-gravel" stacking sintering method[13]. The lithium-rich additive $Li_6Zr_2O_7$ [LiZO, decomposes into $Li_2O + Li_2ZrO_3$ during high temperature sintering (> 1,160 °C)] is selected to compensate for the loss of lithium atmosphere during the sintering process of the green pellets while also enhancing the bonding of grain boundaries and speeding up the ceramic sintering [Scheme 1]. In addition, detailed evaluations on the phase, relative density (RD), conductivity, microstructure, and grain revolution were conducted for ceramics prepared via wet and dry routes under different amounts of LiZO additives. Finally, the electrochemical performance of symmetric and Li-LiFePO$_4$ cells fabricated with Nb-LLZO ceramics produced by the optimized conditions was evaluated to verify the application of these ceramics.

EXPERIMENTAL

Powder and ceramic preparation

Due to the high conductivity and low cost, a composition of Nb-LLZO (0% excessive Li, Li0) and 0/2/4 wt% LiZO (Li0L0/2/4) (Abbreviations and full names summarized in Supplementary Table 1) additive was utilized in this work. The precursors included $LiOH \cdot H_2O$ (Aladdin, AR 98%), ZrO_2 (NanJingMingShan, AR, 99.99%), La_2O_3 (Sinopharm Chemical Reagent, 99.95%), and Nb_2O_5 (Aladdin, 99.9%). The wet route was prepared as follows. Precursor powders with a stoichiometry ratio of Nb-LLZO were ball milled at 180 rpm (revolution) for 3 h with IPA and yttrium-stabilized zirconium oxide (YSZ) beads as the milling media. After drying at 55 °C for 12 h, dried powders were calcinated at 850 °C for 6 h to obtain cubic garnet-phase Nb-LLZO powders. These powders were sieved through P80 mesh and then further ball milled at 150 rpm (revolution) for 3 h to obtain a tailored powder. These fine powders were dried at 55 °C for 6 h and then sieved through 200-grit mesh. Furthermore, 1 g of sieved powder was uniaxially pressed into 12 mm green pellets at 3 tons. The solvent-free method saves solvents and drying processes compared to the wet route and differs in the material of the ball-milling tank. Scheme 2 depicts the preparation process for the conventional wet approach and the solvent-free method (hereafter known as the dry method). Table 1 displays the specific parameters for the dry and wet routes. LiZO powders were prepared by a solid-state reaction. After weighing the raw powders $LiOH \cdot H_2O$ (Aladdin, AR 98%) and ZrO_2 (NanJingMingShan, AR, 99.99%) at the molar ratio of lithium-to-zirconium equal to 4, they were ball-milled for 6 h at 400 rpm (rotation, revolution 200 rpm)[37]. The mixture was dried and calcined at 800 °C for 6 h to obtain the LiZO additive.

Characterizations

The crystal structures of powders and ceramics were characterized through powder X-ray diffraction (XRD) (Rigaku Ultima IV, 40 mA, 40kV) in the range of 10~60° at 8° min^{-1}. The Archimedes method was utilized for calculating the densities of ceramics; pure EA is used as the medium. The theoretical density of Nb-LLZO was 5.14 g cm^{-3}, which is calculated from XRD results. Applying the FullProf software suite, Rietveld co-refinement against XRD patterns was conducted. A scanning electron microscope (SEM, TESCAN-MIRA3) was used to investigate the ceramic's microstructure and the green pellets. The energy dispersive spectrum (EDS, Bruker QUANTAX), which was attached to the SEM, characterized the element mapping and point scanning. The ionic conductivity of ceramics is tested by electrochemical impedance spectroscopy (EIS, Zahner Zennium Pro) with a frequency range of 8 M Hz to 10 Hz or 1 Hz. To confirm the validity of the test, Ag is plated onto ceramic surfaces employing ion sputter (HeTongChuangYe, HTCY, JS-1600) as the blocking electrodes.

Table 1. Preparation process comparison

Parameters	Wet	Dry
Tank material and inner dimensions	Nylon, φ110 × h100 mm	Polyurethane, φ110 × h100 mm
Grinding media	YSZ, φ10 mm × 100 g, φ5 mm × 600 g	
Planetary milling machine	MITR Co Ltd, YXQM-8L. Main disk, φ420 mm	
Mixing weight	~206 g + 400 g IPA	~206 g
Revolution/rotation (mixing)	180/360 r min × 3 h	
Drying (mixing)	55 °C × 12 h	No
Loading in φ95 × h95 mm MgO	120 g	200 g
Calcination	Open crucible, 3 °C min^{-1}, 850 °C × 6 h	
Tailoring weight	80 g Nb4.5Li0 + 0/1.6/3.2 g LiZO + 160 g IPA	80 g Nb4.5Li0 + 0/1.6/3.2 g LiZO
Revolution/rotation (tailoring)	150/300 r min × 3 h	
Drying (tailoring)	55 °C × 6 h	No
Sieving	200 grits, stainless steel screen mesh	
Formation	φ12 mm, 1 g, 3 tons (~265 MPa)	
Sintering	φ25 × h28 mm MgO Crucible & Lid, 7 pellets stack	

$$Li_6Zr_2O_7(LiZO, s) \rightarrow Li_2O(g) + 2Li_2ZrO_3(s)$$
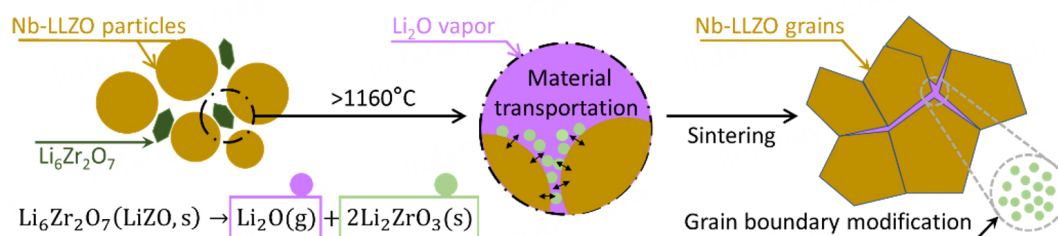
Scheme 1. Schematic illustration of the roles of $Li_6Zr_2O_7$ (LiZO).
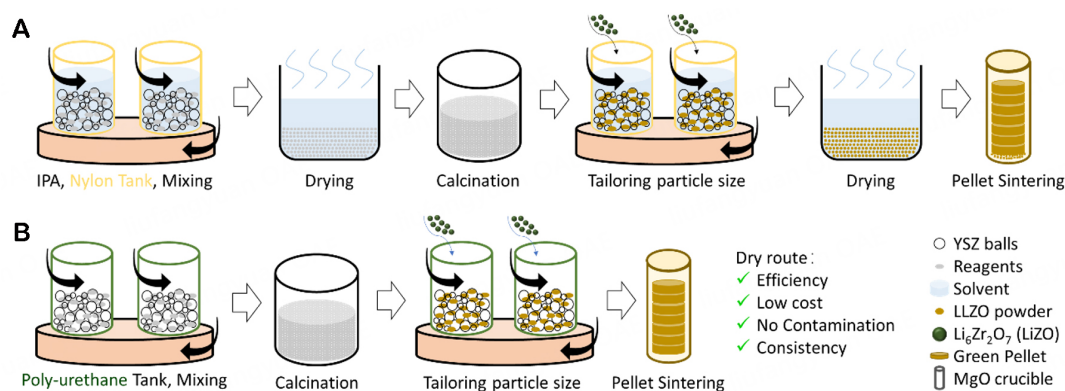
Scheme 2. Schematic diagrams of (A) the conventional wet-milling route and (B) the modified solvent-free route, respectively.

Electrochemical measurements

Dry-processed Nb4.5Li0L2 pellets were ground to parallel surfaces with a thickness of about 2 mm using a 1,200 grit SiC grind disk, and they were subsequently polished to a shine using 1,200 grit abrasive paper. Because of the negative interaction between metallic lithium and Nb-LLZO, there are two different approaches to building Li|Li symmetric cells. Li|Nb-LLZO|Li was assembled by gently rubbing the polished Nb-LLZO in a lithium soup at 330 °C until the ceramic surface was covered with clean molten lithium. As a comparison, two pieces of Li foil (φ10 mm × thickness 100 μm) were attached to the parallel faces, and a

separator is inserted as a barrier between the lithium foil and the ceramic. Additionally, 5 μL(1 M LiPF6 in 1:1 vol/vol EC/DEC) of electrolyte was injected as lubricant on both sides of the separators to improve cycle performance. For Li|LFP full cells, the cathode included 70 wt% active material (70 wt% LFP, 20 wt% super P, 10 wt% PVDF) with an average mass loading of ~3.08 mg cm^{-2}. A small amount of electrolyte (10 μL, 1 M LiPF6 in 1:1 vol/vol EC/DEC) is used to wet the cathode-garnet electrolyte interface. All the symmetrical and full cells are assembled in coin-2032 cells. And to separate water and oxygen, all of the aforementioned activities are completed in a glovebox filled with argon ($O_2 < 0.5$ ppm, $H_2O < 0.1$ ppm).

RESULTS AND DISCUSSION

Precursors mixed using wet and dry processes exhibit various XRD characteristic peaks after calcination [Figure 1] (The standard cubic and tetragonal LLZO XRD patterns are calculated by Diamond software referring to Refs.[39,40].). When LiZO was calcined after 800 °C × 6 h, a negligible quantity of new impurity phases could be observed. The ratio of Li to Zr was 4:1 for the synthesis of LiZO, where the Li_2O was excessive. At this temperature, the vapor pressure of Li_2O is low[41] and there is essentially no extra lithium loss, indicating that the LiZO phase needs additional Li to maintain its main phase. After being calcined at 850 °C × 6 h, the wet-mixed powders showed a pure cubic phase, which was compatible with the findings in prior literature[42,43]. The dry-mixed powder had a wider FWHM, and the peak corresponding to the La_2O_3 raw material phase (PDF # 05-0602) could be observed. This indicated that some of the tough La_2O_3 particles were not thoroughly pulverized and blended during the dry mixing procedure[27]. A small amount of La_2O_3 would not influence the final sintering results[44].

XRD patterns of Li0L0 and Li0L4 powders tailored by dry and wet routes with corresponding Rietveld refinement are shown in Figure 2. Four structure models, including cubic and tetragonal garnet-type LLZO, monoclinic-type LiZO, and trigonal-type La_2O_3, were applied to refine the diffraction data. The phase proportions were listed in Table 2. Minor La_2O_3 phase occurred in all powder refining data, and the dry routes are more apparent than the wet technique for this phenomenon. Cubic LLZO remained the dominant phase in all refinement XRD data, comprising 98% or more. As a result, the main phase is used as the basis for the evaluation of powder lattice parameters in this work (i.e., cubic phase LLZO). Dry ball milling is more effective at breaking the lattice because it is solvent-free, which causes the LLZO particles to undergo amorphization to a greater extent. There was a significant difference in the lattice parameters between fine powders produced by dry and wet routes. The lattice parameters of wet-tailored powders (Li0L0/4 wet) were all higher than 13.0 Å, whereas the lattice values of dry-tailored powders (Li0L0/4 dry) were all near to 12.9 Å. The enlarged lattice after wet tailoring originated from the solvent's absorption of moisture, which introduced serious Li^+/H^+ exchange. Powders in cubic LLZO with less Li^+/H^+ exchange after dry tailoring would benefit the sintering results.

The Thermogravimetric analysis- differential scanning calorimetry (TG-DSC) results of as-tailored Li0L0~4 powders were shown in Figure 3. Obviously, dry and wet tailoring gave the powders different characteristics. For wet tailoring powders, there were five stages of weight loss, whereas just two steps for the dry procedure. When cooled in an ambient setting, the sintered powders will absorb H_2O and CO_2 from the ambient atmosphere, forming chemical adsorption materials on the surface of LLZO[45]. After wet tailoring, the weight loss stages dramatically increased to five in comparison with the dry route, indicating more serious and complex pollution in wet-milled powders. Wet-milling powders lost more weight overall than 10 wt%, indicating a considerable protonation of wet tailored powders[46]. The weight loss of Li0L0 and Li0L4 powders after dry tailoring at stage VII was just 1.5 and 1.16 wt%, proving that the dry route greatly prevented the protonation degradation. Contrary to our expectations, the weight loss ratios for Li0L0 and Li0L4 powders after both wet or dry tailoring showed no correlation with the lithium-rich additive (LiZO).

Table 2. Ratios of c-LLZO and t-LLZO, $Li_6Zr_2O_7$ and La_2O_3 phases

Sample	Cell parameter (Å)	Ratio (%)				Error
	c-LLZO	c-LLZO	t-LLZO	La_2O_3	LiZO	R_{wp}
Nb4.5Li0L0 Wet	13.035	97.87%	1.87%	0.26%	0%	6.39%
Nb4.5Li0L4 Wet	13.020	98.93%	0.11%	0.21%	0.75%	6.11%
Nb4.5Li0L0 Dry	12.901	98.68%	0.72%	0.6%	0%	6.23%
Nb4.5Li0L4 Dry	12.899	97.48%	0.97%	0.8%	0.75%	6.22%
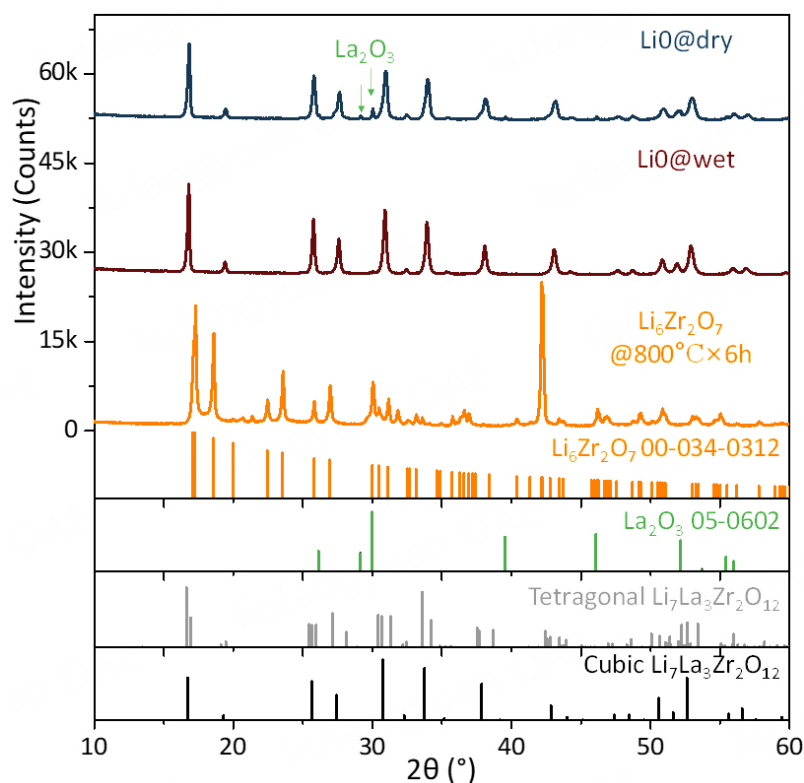
Figure 1. Phase result of sintered powders. XRD patterns of as-calcinated $Li_6Zr_2O_7$ and LiO via wet and dry routes.

Li0L4 powder containing LiZO should lose more weight than Li0L0 because the excessive Li should decompose into additional Li_2O in LiZO powder, which would react with H_2O and CO_2 to form LiOH and Li_2CO_3. It is possible that the extra lithium formed a small amount of other lithium-rich Li-Zr-O species, such as Li_8ZrO_6, whose decomposition temperature is higher than 1,150 °C (LiZO is 1,160 °C)[35]. In addition, the Li^+/H^+ exchange in Li-Zr-O compounds seemed not as serious as that in LLZO, which contributed to the less weight loss of Li0L4-wet/dry powders than that of Li0L0-wet/dry. Dry milled Li0L4 powder was expected to deliver the best sintering result due to less contamination and plenty of *in-situ* Li_2O atmosphere.

Figure 4 shows the cross-sectional morphology of the as-sintered Li0L0 and Li0L4 pellets, proving the good sintering results for dry milled Li0L4 powder. Both the dry and wet milled Li0L0 cannot be densified at 1,220 °C, where many worm-like grains with rough surfaces and lots of pores occurred [Supplementary Figure 1]. The absence of plenty of Li_2O environment[23] inhibited the densification of wet/dry milled Li0L0 [Supplementary Figures 2 and 3]. In stark contrast, the RD of the dry milled Li0L4 was as
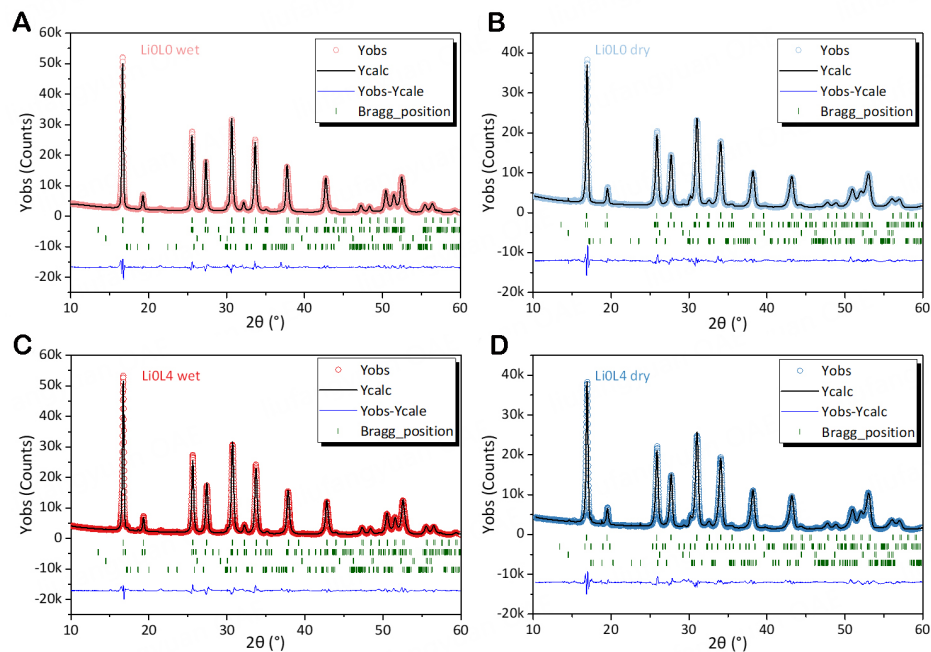
Figure 2. Refinement profiles of XRD data of (A) Li0L0 wet, (B) Li0L0 dry, (C) Li0L4 wet, and (D) Li0L4 dry powders. The software applied for Refinement is Fullprof suite. The CIF files adopted for refinement are La_2O_3, $Li_6Zr_2O_7$, tetragonal LLZO, and cubic LLZO from the COD database.
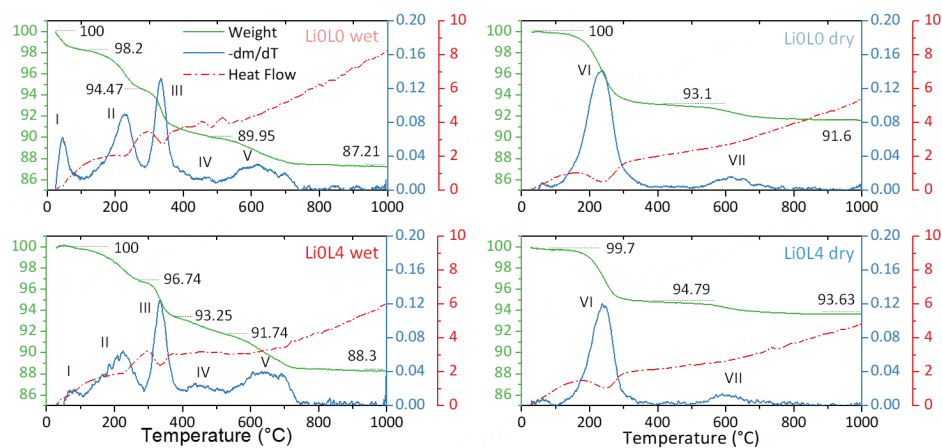

Figure 3. TG-DSC of Li0L0 and Li0L4 powders treated with wet-dry routes. The purge gas is 80% N_2 and 20% O_2 monitoring the practical calcination and sintering under ambient air. The I~VII stages corresponded to the following reactions: I: 20~60 °C, CH_3CHOH CH_3 (l) $\rightarrow$ $CH_3CHOHCH_3$ (g); II: 80~230 °C, $LiOH\cdot H_2O$ $\rightarrow$ $LiOH\cdot0.5H_2O + H_2O$ (g), H_2O (Absorbed) $\rightarrow$ H_2O (g), CO_2 (Absorbed) $\rightarrow$ CO_2 (g); III: 230~330 °C, $Li_{6.55-x}H_xLa_3Zr_{1.55}Nb_{0.45}O_{12}$ $\rightarrow$ H_2O (g) + Decompositions; IV: 330~500 °C, $Li_{6.55-x}H_xLa_3Zr_{1.55}Nb_{0.45}O_{12}$ $\rightarrow$ $0.5xH_2O$ (g) + $Li_{6.55-x}La_3Zr_{1.55}Nb_{0.45}O_{12-0.5x}$, $LiOH\cdot0.5H_2O$ $\rightarrow$ $LiOH + H_2O$ (g); V: 500~1,000 °C, $LiOH$ $\rightarrow$ $0.5Li_2O + 0.5H_2O$ (g), Li_2CO_3 $\rightarrow$ $Li_2O + CO_2$ (g); VI: 150~280 °C, H_2O (Absorbed) $\rightarrow$ H_2O (g), CO_2 (Absorbed) $\rightarrow$ CO_2 (g), $Li_{6.55-x}H_xLa_3Zr_{1.55}Nb_{0.45}O_{12}$ $\rightarrow$ H_2O (g) + Decompositions; VII: 300~1,000 °C, Li_2CO_3 $\rightarrow$ $Li_2O + CO_2$ (g).

high as 96.45%. The decomposition of LiZO produced an *in-situ* Li_2O atmosphere, which served the same role as mother powder in promoting the sintering[47]. When the sintering temperature reached 1,260 °C, the RDs of the dry milled Li0L0 and Li0L4 ceramics were 93.75% and 95.60%, respectively, which were much higher than that of the wet milled Li0L0 and Li0L4 (90.48% and 94.14%). In addition, the wet milled Li0L4
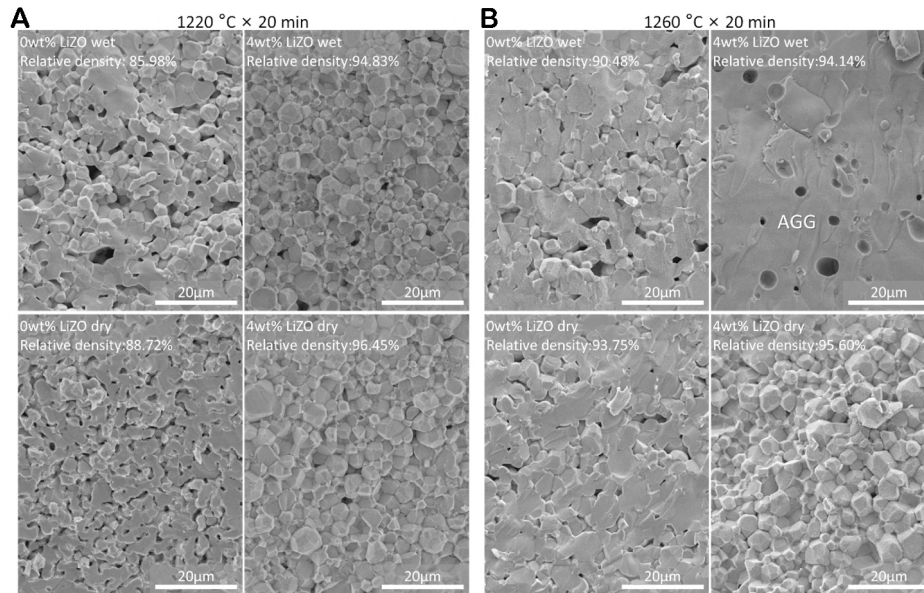
Figure 4. Cross-section SEM images of the Li0L0 and Li0L4 pellets sintered at (A) 1,220 °C × 20 min, (B) 1,260 °C × 20 min.

contained huge grains, whereas the dry milled Li0L4 contained uniform grains. The vapor pressure of Li_2O increases more rapidly compared to LLZO, allowing the high-sintering activity LLZO particles prepared by the wet route to grow rapidly, leading to the formation of an abnormal grain growth (AGG) phenomenon. Contaminations in wet milled Li0L4 powders contributed to the poor densification of corresponding ceramics. Nevertheless, LiZO effectively provided the Li_2O atmosphere for densification, and dry milling strategy ensured the dense ceramic after sintering.

Nyquist plots of as-sintered L0/4- wet/dry ceramics further proved the effect of Li_2O atmosphere *in-situ* provided by $Li_6Zr_2O_6$. Li0L0 ceramic sintered at 1,220 °C contained two semicircles [Figure 5A], which corresponded to the grains and grain boundaries, respectively. The inflection point between the first and second semicircle for Li0L0 was 215 kHz, where this point was defined as the terminal frequency (TF). Dry-processed ceramics had a much higher TF than that of wet-processed ceramics in the second flat semicircle in the mid-low frequency range, where all ceramics sintered at 1,220~1,280 °C exhibited this feature [Figure 5A and B, Supplementary Figure 4A and C]. The TF was positively related to the rate of Li^+ migration at the grain boundaries[48]. The low TF in all Li0-wet ceramics indicated the sluggish Li^+ migration across the grain boundaries, which originated from the lack of Li_2O and the deterioration of contaminations introduced in wet milling. Comparatively, the second semicircle disappeared in Li0L4-wet/dry ceramics [Figure 5A and B, Supplementary Figure 4B and D]. The characteristic relaxation times corresponding to LLZO grain and grain boundaries were so close to each other that Li0L4 ceramics with tight grain boundaries exhibited no distinguishable two semicircles in Nyquist plots[49]. Herein, the Nyquist plots of Li0L0 and Li0L4 ceramics sintered at 1,220~1,280 °C were fitted using the distribution of relaxation times (DRT). It is a mathematical modification to display the frequency domain-based Nyquist plots into time domain-based DRT spectra[50,51] as follows: $Z(\omega) = R_\infty + \int_0^\infty \frac{\gamma(\tau)}{1+j\omega\tau} d\tau$, where R_∞ denotes the ohmic resistance, $\gamma(\tau)$ is the distribution function of relaxation time, and τ is the relaxation time. As shown in Figure 5C and D, the Li0L0 clearly contained two characteristic peaks belonging to grains and grain boundaries, whereas Li0L4 contained only one peak, which was similar to the one peak observed for Ta-doped LLZO[27]. As illustrated in Figure 5E and F, distinctive resistances contributed by grains and grain boundaries were calculated from
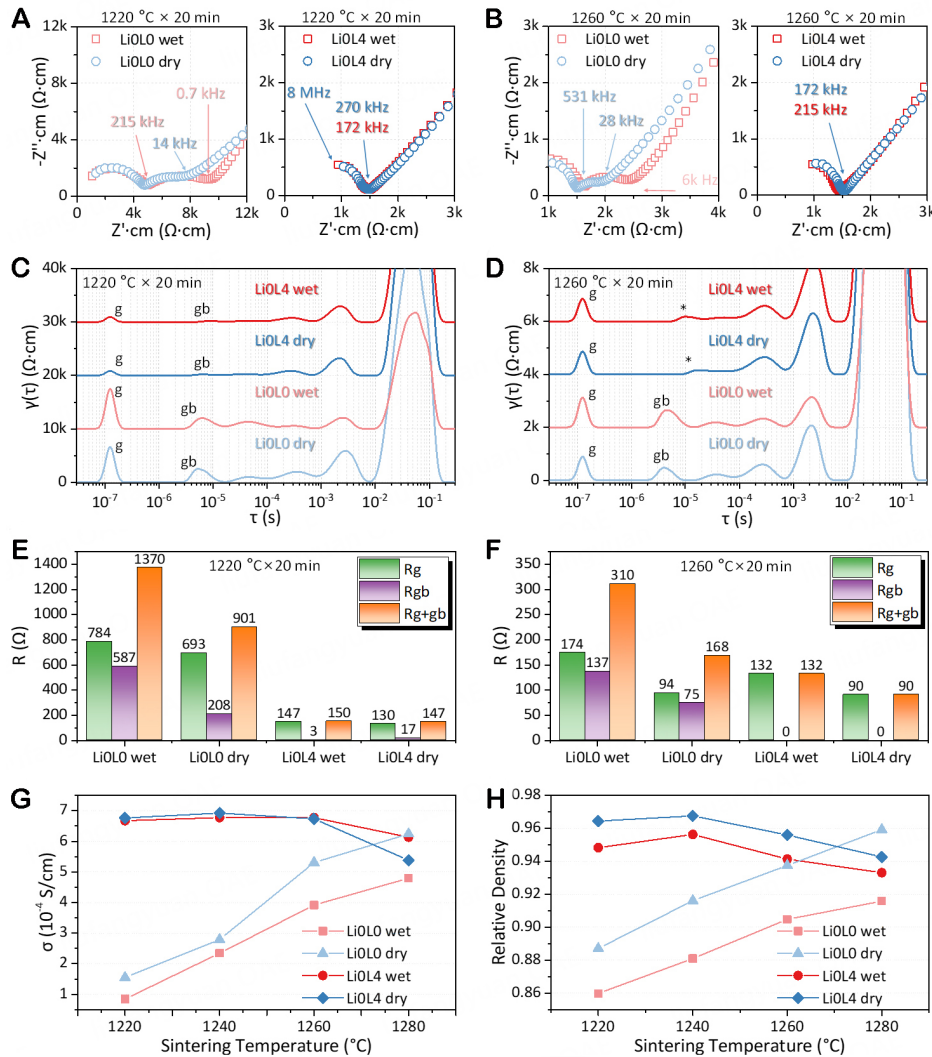
Figure 5. Normalized Nyquist plots of Li0L0/4 ceramics sintered at (A) 1,220 °C × 20 min and (B) 1,260 °C × 20 min. (C and D) DRT transition of Nyquist plots. g: grain, bulk. gb: grain boundary. (E and F) Resistance data calculated from the DRT results. (G) Li$^+$ conductivities and (H) Relative densities of Li0L0/4 sintered at 1,220-1,280 °C for 20 min.

DRT peaks. The Li0L0-wet sintered at 1,220 °C delivered the maximum total, Rg and Rgb resistances. The Rg of Li0L0-dry was 693 Ω, while the Rgb of 208 Ω was only half of that of Li0L0-wet. Rg and Rgb of Li0L0 tended to decrease with elevated sintering temperature, whereas Rgb could not be diminished. Compared to Li0L0 samples, the Rg and Rgb of Li0L4 were much lower than that of Li0L0, where the grain boundary impedance of Li0L4 samples could be decreased to 0.

Figure 5G and H depicts the conductivities and RD of Li0L0/4 ceramics at room temperature (23.7 °C). The RD and conductivity of all Li0L0 samples improved with increasing sintering temperature, whereas the Li0L4 exhibited a decreasing trend above 1,240 °C. The conductivities of Li0L4 ceramics maintained above 6 × 10^{-4} S cm^{-1}, where no distinction occurred between samples processed via dry or wet milling. The RD of ceramics prepared by a dry route was approximately 2% higher than that prepared by a wet route within all sintering temperatures, proving the advantages of fewer contaminations of the dry route. An RD of no more than 90% represents a loose microstructure, where loose grain boundaries make the migration of Li$^+$

difficult, resulting in low ionic conductivity. Therefore, the conductivity of Li0L0-dry samples is higher than Li0L0-wet samples at 1,220~1,280 °C sintering. Due to the absence of Li_2O atmosphere, Li0L0 pellets could only be densified at a high temperature of 1,280 °C, whereas high impedance contributed by grain boundaries could not be diminished, as shown in Supplementary Figures 4 and 5. Li0L4 ceramics could well be densified at a relatively low temperature. The vapor pressure of Li_2O generated from LiZO increased much higher than that of Nb-LLZO when the sintering temperature was raised to over 1,200 °C[35], which promoted sintering.

As shown in Figure 6, the evolution of grain and grain boundaries was studied to reveal the advantages of LiZO additive during the dry route. The densification procedure for Nb-LLZO was divided into six stages from green pellet to dense ceramic. Numerous amorphous, glassy substances with dark hues were found among grains in wet ball-milling powders [Figure 6B and D]. Deep protonated LLZO after wet milling would first decompose at 300-700 °C and then react with Li-rich contaminations at 700-1,000 °C during the sintering process[45], which hindered densification. Compared to the particles contaminated with solvents, dry milled powders were clean, indicating the few contaminations. When sintered at 1,080 °C for one minute (Stage 2), where the lithium-rich additive LiZO did not release Li_2O, all particles had grown with small necks developing between grains. Wet processed samples delivered a lower density than dry processed samples. The green pellets pressed from dry milled powder usually delivered high densities due to the few contaminations in powders. As the temperature increased to over 1,160 °C (Stage 3), cross-sectional microstructures of Li0L0 and Li0L4 ceramics differed substantially. The grains in Li0L4 grew significantly large with clear polyhedron surfaces and obvious linking necks. In contrast, the grains of the Li0L0 samples almost retained the same shape as that in stage 2. At stage 4, Li0L4 densified more with well-developed edges and distinct grain boundaries. In contrast, the Li0L0 grains failed to form a unique polyhedral shape, and they began to join with each other. At stage 5, the grains of Li0L4 further developed. The Li0L4-dry ceramic was almost densified while the Li0L4-wet ceramic contained lots of pores. In contrast, the Li0L0 ceramics exhibited trans-granular fractures, indicating the weak bulk strength, which might originate from the lack of Li in the LLZO lattice. At stage 6, grains in Li0L4-dry were tightly connected with clear grain boundaries and few isolated pores. In Li0L4-wet, the pores could not be completely evacuated. Li0L0 dry reached a relatively tight cross-sectional microstructure in trans-granular fracture at a high temperature of 1,300 °C, whereas Li0L0-wet exhibited abnormally grown grains with a great number of pores.

The evolution of ceramic microstructures explicated the role of LiZO in ceramic sintering: promoting the grain growth and enhancing grain boundary adhesion. The influence of dry and wet routes on particles was also clearly demonstrated: ceramics manufactured by the dry route could achieve a higher density than that by the wet route. Li0L4-dry required just 1,220 °C × 1 min to reach an RD higher than 90%. As shown in Figure 7, the changes in the RD and ion conductivity of the samples correlated to their microstructures.

The role of LiZO at grain boundaries was further revealed by EDS, as shown in Figure 8. A typical triangular grain boundary with glue-like segregations was selected to show the distributions of La, Zr, Nb, and O. Figure 8B depicted the element ratios at points 1, 2, and 3. Zr, La, and O ratios at bulk grains (point 3, 11.4%, 16.2%, and 67.8%, respectively) were similar to stoichiometric Nb-LLZO. The Zr ratio at the grain boundary was doubled (19.4%) to the ratio at the bulk grains. Additionally, the Zr-O ratio of the two kinds of sites ranged between 1:3 (point 3) and 2:7 (points 1 and 2); the second phase at the grain boundary was predominantly composed of Li_2ZrO_3 or LiZO species. A small excess of Nb may originate from the formation of Li_xNbO_y from Li_2O and Nb during sintering[27].
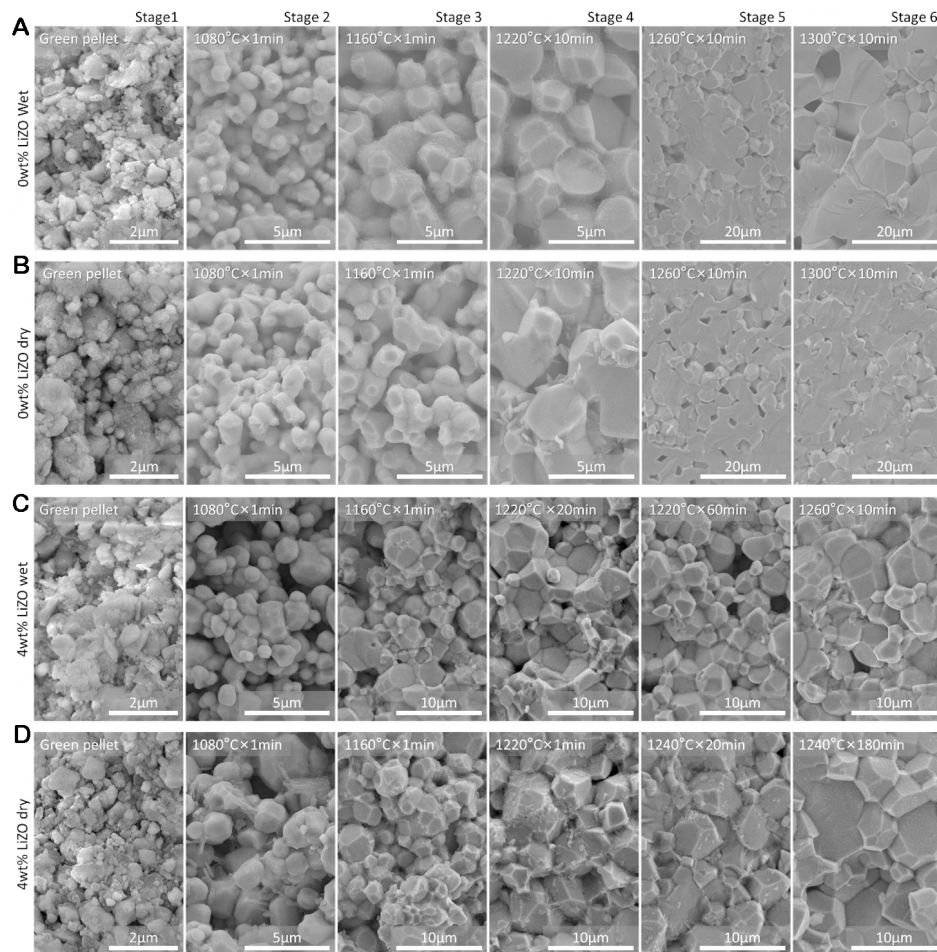
Figure 6. Evolution of the grain morphology. Cross-sectional SEM images of Nb-LLZO pellets: (A) Li0L0 wet, (B) Li0L0 dry, (C) Li0L4 wet, and (D) Li0L4 dry.
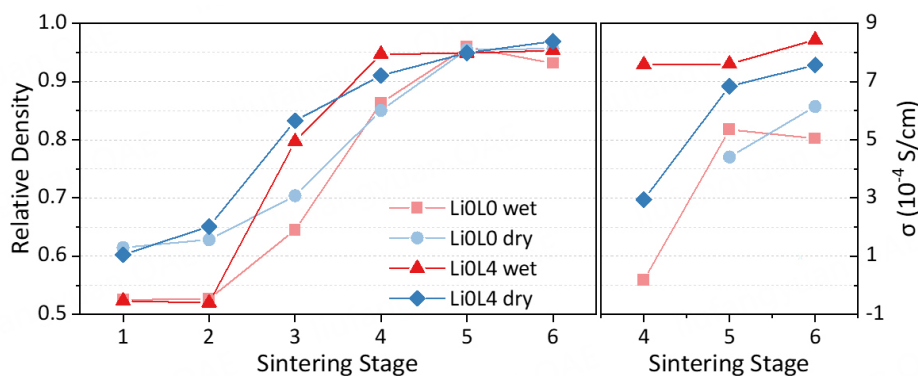

Figure 7. Conductivity and relative density of Nb-LLZO ceramics shown in Figure 6.

Cross-sectional triangular grain boundaries were further characterized by X-ray photoelectron spectroscopy (XPS) [Figure 9]. The ceramic sample was sintered at 1,220 °C × 1 min and then was prepared inside an Ar-filled glovebox avoiding the contamination from trace-level H_2O and CO_2. Ar^+ sputtering was performed on the surface of the stripped LLZO to remove contamination before test. And due to the unevenness of the
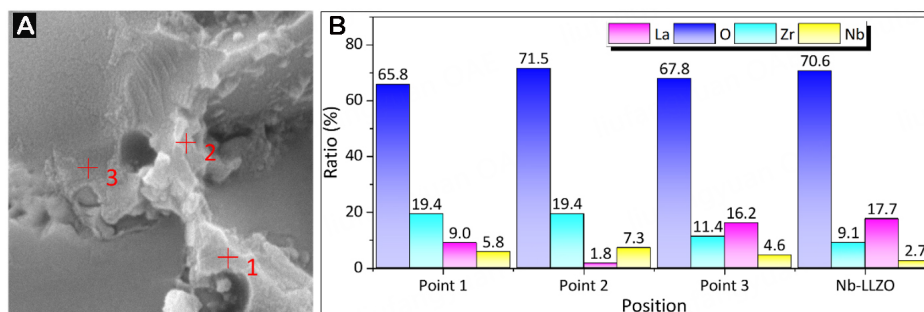
Figure 8. Second phase species analysis at grain boundary. (A) cross-sectional SEM images of Li0L4 dry ceramics. (B) element analysis results of points at the triple-point grain boundary and grain.
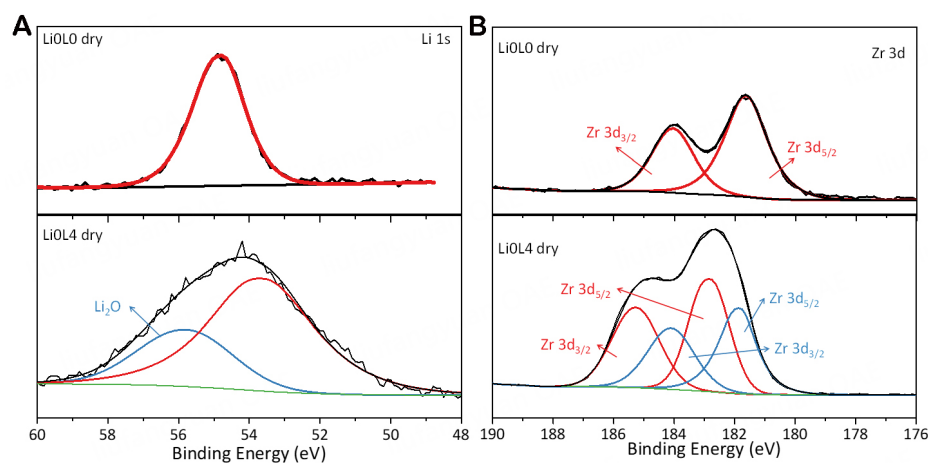

Figure 9. Second phase species analysis at grain boundary. XPS spectra of (A and B) Li 1s, Zr 3d of the cross-section pellets for Li0L0 dry and Li0L4 dry.

ceramic cross-section, the binding energy of elements might be partially shifted. The O 1s peak at 54.9 eV in Li0L0 dry represents the Nb-LLZO[52]. The O 1s spectra of Li0L4 dry were deconvoluted into two peaks at 53.7 and 55.9 eV corresponding to Nb-LLZO and Li_2O, respectively[53]. In Figure 9B, all Zr 3d spectra exhibited a doublet with a fixed difference of 2.43 eV due to the spin-split coupling between $3d_{5/2}$ and $3d_{3/2}$. For dry Li0L0, just one chemical environment peak of Zr could be identified, which corresponded to the Zr in cubic LLZO[53,54]. The Zr 3d spectrum of the Li0L4 sample exhibited evident distortion and widening, revealing two different chemical environments of Zr. The main peak of Zr $3d_{5/2}$ located at the 182.8 eV corresponds to the Zr in the cubic LLZO while the side peak of the Zr $3d_{5/2}$ at the 181.8 eV was ascribed to the Li-Zr-O (e.g., Li_2ZrO_3)[55,56] at the cross-section of the sample. The Li-Zr-O could not be detected in the Raman test [Supplementary Figure 6], which originated from the small amount of Li-Zr-O existing at the narrow grain boundaries. Nevertheless, these results further proved the decomposition of LiZO to Li_2O and Li-Zr-O at the grain boundaries.

The production of LLZO ceramic pellets was conducted by applying Li0L2 as the composition via a solvent-free method. Li0L4 was not adopted due to the relatively low conductive decomposed Li-Zr-O compounds. Plenty of Li-Zr-O compounds *in-situ* formed at grain boundaries could improve the robustness of controlling the grain growth; however, these materials would hinder the Li⁺ transportation across the grain boundaries. Figure 10A depicted the RD of seven parallel samples of Li0L2 sintered by four sintering conditions. All these samples had an RD higher than 96%. The consistency was examined using standard
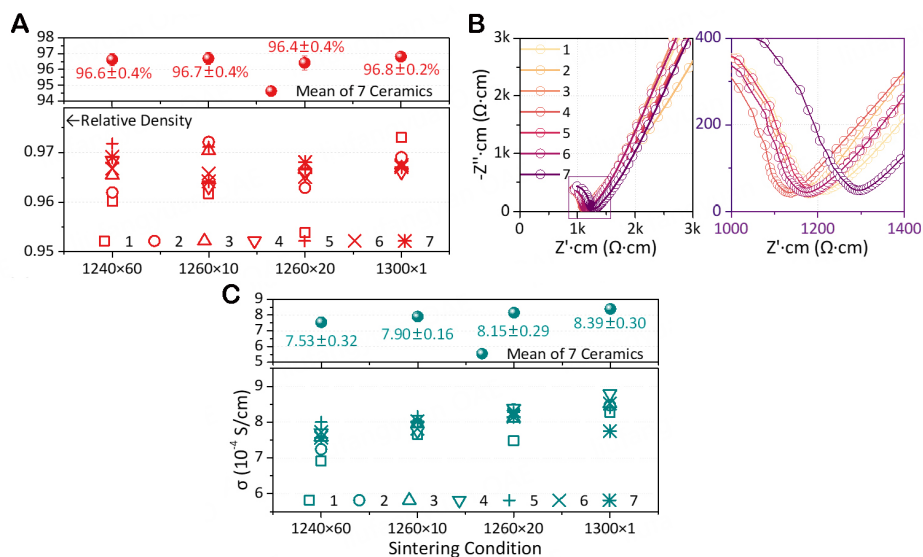
Figure 10. Inspection concerning consistency of as-produced ceramics. Consistency and mean/standard deviation in (A) relative densities, (B) Nyquist plots of LiOL2 dry sintered at 1,300 °C × 1 min, and (C) Li$^+$ conductivities of LiOL2 dry pellets.

deviation (S.D.). Clearly, the average RD of ceramics manufactured by dry method was high with low S.D. This consistency was also proved in EIS. Figure 10B depicted the Nyquist plots (25 °C) of Li0L2-dry sintered at 1,300 °C for 1 min, and Supplementary Figure 7 depicted the data for other samples. All the plots delivered only one semicircle corresponding to dense microstructure. All parallel pellets in each group sintered under four conditions showed high consistency. The Li0L2-dry sintered at 1,300 °C for 1 min had the highest RD and conductivity [Figure 10C] of 96.8% and 8.39 × 10^{-4} S cm^{-1}, respectively. The RD and conductivities of these parallel pellets sintered at different positions inside the MgO crucible were shown in Supplementary Figure 8.

Figure 11A and B showed the Nyquist plots of the above Li0L2-dry ceramics measured at -20 to 60 °C. By linearly fitting the Arrhenius plots [Figure 11C], the activation energy calculated from the total conductivity is 0.441 eV[57]. Highly conductive LLZO ceramics in good consistency could be produced with the aid of LiZO and a dry route. As a product, Nb-LLZO SE Li0L2 delivered high consistency in high RD (~97%) and conductivity (> 8 × 10^{-4} S cm^{-1}).

Because the Nb-LLZO is unstable against lithium metal[58-60], the Li|Nb-LLZO|Li cells soon (no more than 50 h) short-circuited at 0.05 mA cm^{-2} [Supplementary Figure 9]. Therefore, as-produced Li0L2-dry pellets were fabricated into Li|LE (liquid electrolyte) |Nb-LLZO|LE (liquid electrolyte) |Li symmetric cells. The Nyquist plot of a symmetric cell was shown in Supplementary Figure 10. The interface impedance was calculated to be 252 Ω cm^{-2}. The Li|LE|Nb-LLZO|LE|Li symmetric cells achieved good cycling stability of 2,000 h [Figure 12A and B]. The critical current density (CCD) performance [Figure 12C] of the Li0L2-dry was as high as 0.9 mA cm^{-2} under a time-fixed testing method. Using capacity-constant mode and keeping the capacities at 0.1 mAh, the cell operated well at 0.1 to 2 mA cm^{-2} [Supplementary Figure 11]. Figure 12D and E shows the rate performance of the Li|LFP cell, which exhibits reversible discharge capacities of 147, 140, 120, and 92 mAh g^{-1}, in line with current densities of 0.1, 0.2, 0.5, and 1 C, respectively. The discharge capacity increased to 136 mAh g^{-1} and cycled continuously for more than 200 cycles when the rate dropped to 0.2 C. The galvanostatic charge/discharge performance of the Li|LFP cell at 0.1 C, with weak attenuation over 150 cycles [Supplementary Figure 12]. In addition, the Li|LFP full cells
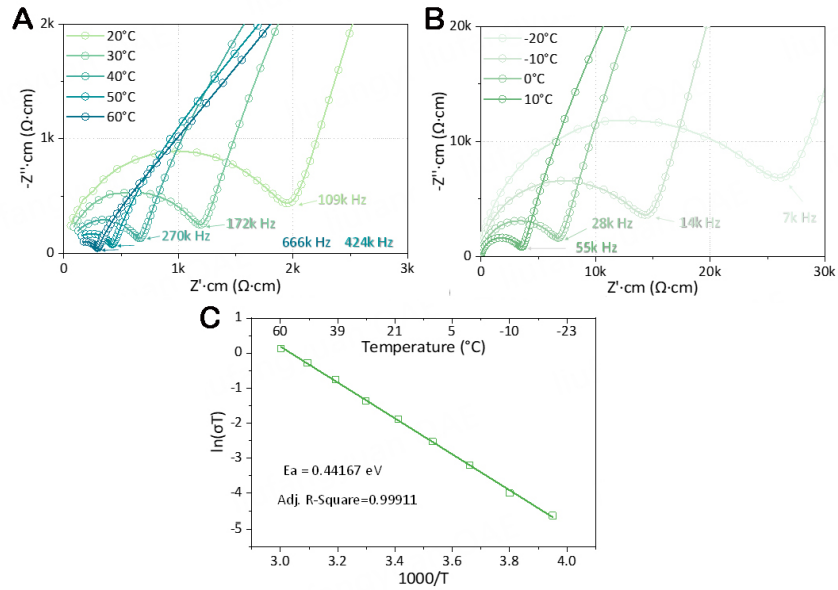
Figure 11. (A and B) Nyquist plots and (C) Arrhenius plot of the mass-produced LiOL2 dry ceramics at -20 to 60 °C.

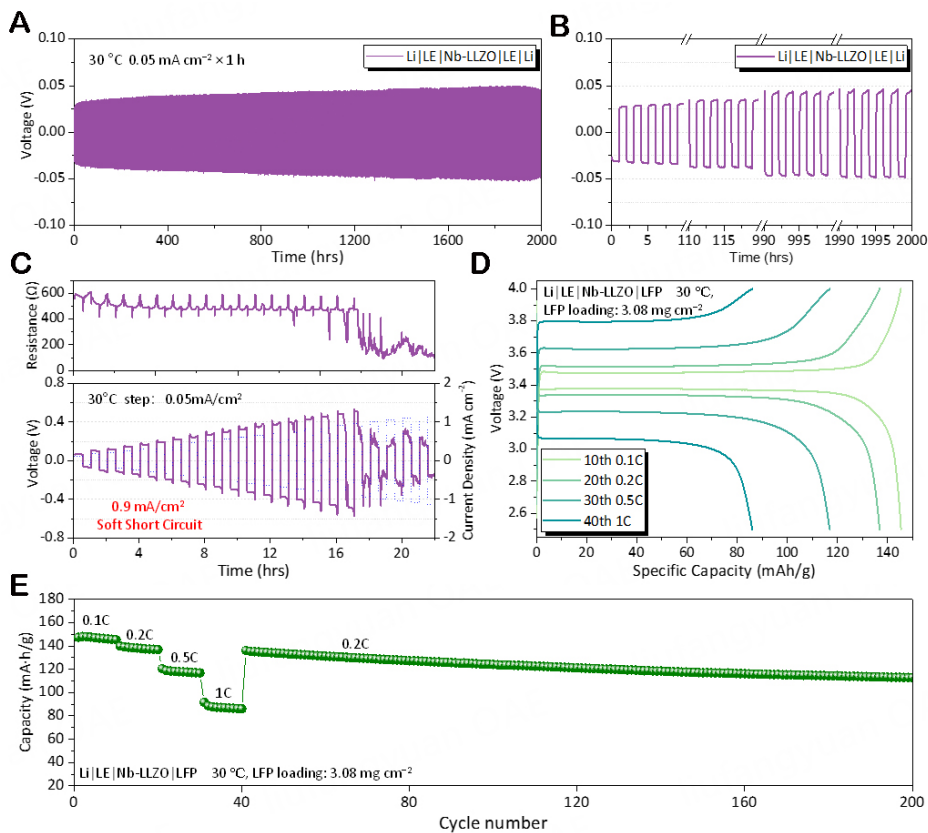**Figure 12.** Electrochemical performances (30 °C) of symmetric Li-Li and full Li-LFP cells fabricated with scalable prepared LiOL2-dry pellets sintered at 1,300 °C for 1 min. (A) Galvanostatic cycling performance of Li-Li symmetric cell, (B) segmental voltage profile of (A), (C) rate performance of Li-Li symmetric cell, (D) voltage profiles and (E) galvanostatic cycling performance of Li-LFP batteries at different rates.

guaranteed a high Coulombic efficiency of over 99% during all cycles. The use of the laboratory-scale produced Li0L2-dry ceramics is demonstrated by the results of the Li|LFP battery and Li|Li symmetric cell.

CONCLUSIONS

The role of lithium-rich additive LiZO was demonstrated in densifying garnet Nb-LLZO. The LiZO decomposed at grain boundaries during sintering, generating a Li_2O environment that enhanced garnet sintering and offset Li-loss. After LiZO decomposition, Li_2ZrO_3 in amorphous and crystalline mixed phases spread along grain boundaries and acted as a bridge to fill the adjacent grain boundaries to improve conductivity. This work developed an economical, efficient route based on solid-state reaction to synthesize LLZO SE. The solvent-free technique avoided contamination caused by solvent-adsorbed contaminants. Increased milling energy, slightly decreased sintering activity, and increased compaction density could be achieved in the dry route for LLZO powders and green pellets. These features enabled LLZO ceramics produced via a solvent-free route to be denser than those produced by a typical wet route. Combining the above *in-situ* Li_2O compensating strategy and solvent-free dry method, grain boundaries in as-produced ceramics were strongly bonded in uniform sizes without AGG. The as-synthesized Nb-LLZO with 2 wt% LiZO additional exhibited a high room-temperature ionic conductivity of 8.39×10^{-4} S cm^{-1} at 25 °C, an RD of 96.8%, and high critical current densities of 0.9 mA cm^{-2} at 30 °C as prepared. Moreover, the ceramics produced in such a batch exhibit an exceptionally high degree of consistency. This work provided an effective production strategy for LLZO ceramics with high performance and high consistency, which promotes the development of solid-state batteries based on garnet-type ceramics.

DECLARATIONS

Authors' contributions
Directed concentration, methodology, formal analysis, data collection, writing (original draft), and investigation: Tang J
Conducted basic characterization and data collection: Zhou Y, Li X
Managed financial support: Tang W
Contributed to conception, methodology, formal analysis, writing-review and editing: Huang X
Responsible for the laboratory platform, supervision, and writing (review and editing): Tian B

Availability of data and materials
The data supporting our findings can be found in the Supplementary Material.

Financial support and sponsorship

Conflicts of interest
All authors declared that there are no conflicts of interest.

Ethical approval and consent to participate
Not applicable.

Consent for publication
Not applicable.

Copyright

© The Author(s) 2024.

REFERENCES

1. Xu L, Lu Y, Zhao C, et al. Toward the scale-up of solid-state lithium metal batteries: the gaps between lab-level cells and practical large-format batteries. *Adv Energy Mater* 2021;11:2002360. DOI
2. Wang MJ, Kazyak E, Dasgupta NP, Sakamoto J. Transitioning solid-state batteries from lab to market: linking electro-chemo-mechanics with practical considerations. *Joule* 2021;5:1371-90. DOI
3. Kim A, Woo S, Kang M, Park H, Kang B. Research progresses of garnet-type solid electrolytes for developing all-solid-state Li batteries. *Front Chem* 2020;8:468. DOI PubMed PMC
4. Li L, Duan H, Li J, Zhang L, Deng Y, Chen G. Toward high performance all-solid-state lithium batteries with high-voltage cathode materials: design strategies for solid electrolytes, cathode interfaces, and composite electrodes. *Adv Energy Mater* 2021;11:2003154. DOI
5. Alexander GV, Indu MS, Murugan R. Review on the critical issues for the realization of all-solid-state lithium metal batteries with garnet electrolyte: interfacial chemistry, dendrite growth, and critical current densities. *Ionics* 2021;27:4105-26. DOI
6. Ramakumar S, Deviannapoorani C, Dhivya L, Shankar LS, Murugan R. Lithium garnets: synthesis, structure, Li^+ conductivity, Li^+ dynamics and applications. *Pro Mater Sci* 2017;88:325-411. DOI
7. Liang L, Sun X, Zhang J, et al. Sur-/interfacial regulation in all-solid-state rechargeable Li-ion batteries based on inorganic solid-state electrolytes: advances and perspectives. *Mater Horiz* 2019;6:871-910. DOI
8. Peng L, Ren H, Zhang J, et al. $LiNbO_3$-coated $LiNi_{0.7}Co_{0.1}Mn_{0.2}O_2$ and chlorine-rich argyrodite enabling high-performance solid-state batteries under different temperatures. *Energy Stor Mater* 2021;43:53-61. DOI
9. He Z, Zhang Z, Yu M, et al. Synthetic optimization and application of Li-argyrodite Li_6PS_5I in solid-state battery at different temperatures. *Rare Met* 2022;41:798-805. DOI
10. Huang X, Lu Y, Song Z, Xiu T, Badding ME, Wen Z. Preparation of dense Ta-LLZO/MgO composite Li-ion solid electrolyte: sintering, microstructure, performance and the role of MgO. *J Energy Chem* 2019;39:8-16. DOI
11. Huang X, Su J, Song Z, et al. Synthesis of Ga-doped $Li_7La_3Zr_2O_{12}$ solid electrolyte with high Li^+ ion conductivity. *Ceram Int* 2021;47:2123-30. DOI
12. Iriyama Y, Wadaguchi M, Yoshida K, Yamamoto Y, Motoyama M, Yamamoto T. 5V-class bulk-type all-solid-state rechargeable lithium batteries with electrode-solid electrolyte composite electrodes prepared by aerosol deposition. *J Power Sources* 2018;385:55-61. DOI
13. Huang X, Tang J, Zhou Y, et al. Developing preparation craft platform for solid electrolytes containing volatile components: experimental study of competition between lithium loss and densification in $Li_7La_3Zr_2O_{12}$. *ACS Appl Mater Interfaces* 2022;14:33340-54. DOI
14. Thompson T, Yu S, Williams L, et al. Electrochemical window of the Li-ion solid electrolyte $Li_7La_3Zr_2O_{12}$. *ACS Energy Lett* 2017;2:462-8. DOI
15. Ma C, Cheng Y, Yin K, et al. Interfacial stability of Li metal-solid electrolyte elucidated via in situ electron microscopy. *Nano Lett* 2016;16:7030-6. DOI
16. Huang X, Xiu T, Badding ME, Wen Z. Two-step sintering strategy to prepare dense Li-Garnet electrolyte ceramics with high Li^+ conductivity. *Ceram Int* 2018;44:5660-7. DOI
17. Awaka J, Kijima N, Hayakawa H, Akimoto J. Synthesis and structure analysis of tetragonal $Li_7La_3Zr_2O_{12}$ with the garnet-related type structure. *J Solid State Chem* 2009;182:2046-52. DOI
18. Wolfenstine J, Rangasamy E, Allen JL, Sakamoto J. High conductivity of dense tetragonal $Li_7La_3Zr_2O_{12}$. *J Power Sources* 2012;208:193-6. DOI
19. Ohta S, Kobayashi T, Asaoka T. High lithium ionic conductivity in the garnet-type oxide $Li_{7-X} La_3(Zr_{2-X}, Nb_X)O_{12}$ (X=0-2). *J Power Sources* 2011;196:3342-5. DOI
20. Li Y, Wang C, Xie H, Cheng J, Goodenough JB. High lithium ion conduction in garnet-type $Li_6La_3ZrTaO_{12}$. *Electrochem Commun* 2011;13:1289-92. DOI
21. Allen J, Wolfenstine J, Rangasamy E, Sakamoto J. Effect of substitution (Ta, Al, Ga) on the conductivity of $Li_7La_3Zr_2O_{12}$. *J Power Sources* 2012;206:315-9. DOI
22. Kotobuki M, Kanamura K, Sato Y, Yoshida T. Fabrication of all-solid-state lithium battery with lithium metal anode using Al_2O_3-added $Li_7La_3Zr_2O_{12}$ solid electrolyte. *J Power Sources* 2011;196:7750-4. DOI
23. Huang X, Lu Y, Song Z, et al. Manipulating Li_2O atmosphere for sintering dense $Li_7La_3Zr_2O_{12}$ solid electrolyte. *Energy Stor Mater* 2019;22:207-17. DOI
24. Huang X, Lu Y, Guo H, et al. None-mother-powder method to prepare dense Li-garnet solid electrolytes with high critical current density. *ACS Appl Energy Mater* 2018;1:5335-65. DOI
25. Nguyen MH, Park S. Synergetic effect of Li-ion concentration and triple doping on ionic conductivity of $Li_7La_3Zr_2O_{12}$ solid electrolyte. *Nanomaterials* 2022;12:2946. DOI PubMed PMC
26. Zhou Y, Li X, Yang Y, Huang X, Tian B. Production of Ta-doped $Li_7La_3Zr_2O_{12}$ solid electrolyte with high critical current density. *ACS*

Appl Energy Mater 2022;5:13817-28. DOI

27.　Huang X, Lu Y, Niu Y, et al. From protonation & Li-rich contamination to grain-boundary segregation: evaluations of solvent-free vs. wet routes on preparing $Li_7La_3Zr_2O_{12}$ solid electrolyte. *J Energy Chem* 2022;73:223-39. DOI

28.　Smetaczek S, Limbeck A, Zeller V, et al. Li^+/H^+ exchange of $Li_7La_3Zr_2O_{12}$ single and polycrystals investigated by quantitative LIBS depth profiling. *Mater Adv* 2022;3:8760-70. DOI PubMed PMC

29.　Arinicheva Y, Guo X, Gerhards M, et al. Competing effects in the hydration mechanism of a garnet-type $Li_7La_3Zr_2O_{12}$ electrolyte. *Chem Mater* 2022;34:1473-80. DOI

30.　Nie K, Wu S, Wang J, et al. Reaction mechanisms of Ta-substituted cubic $Li_7La_3Zr_2O_{12}$ with solvents during storage. *ACS Appl Mater Interfaces* 2021;13:38384-93. DOI

31.　Gupta A, Kazyak E, Dasgupta NP, Sakamoto J. Electrochemical and surface chemistry analysis of lithium lanthanum zirconium tantalum oxide (LLZTO)/liquid electrolyte (LE) interfaces. *J Power Sources* 2020;474:228598. DOI

32.　Wood M, Gao X, Shi R, et al. Exploring the relationship between solvent-assisted ball milling, particle size, and sintering temperature in garnet-type solid electrolytes. *J Power Sources* 2021;484:229252. DOI

33.　Zheng H, Li G, Liu J, et al. A rational design of garnet-type $Li_7La_3Zr_2O_{12}$ with ultrahigh moisture stability. *Energy Stor Mater* 2022;49:278-90. DOI

34.　Zheng H, Li G, Liu H, Wu Y, Duan H. Influence of dry- and wet-milled LLZTO particles on the sintered pellets. *J Am Ceram Soc* 2023;106:274-84. DOI

35.　Huang X, Song Z, Xiu T, Badding ME, Wen Z. Searching for low-cost Li_xMO_y compounds for compensating Li-loss in sintering of Li-Garnet solid electrolyte. *J Materiomics* 2019;5:221-8. DOI

36.　Murugan R, Thangadurai V, Weppner W. Fast lithium ion conduction in garnet-type $Li_7La_3Zr_2O_{12}$. *Angew Chem Int* 2007;46:7778-81. DOI PubMed

37.　Zheng C, Ruan Y, Su J, et al. Grain boundary modification in garnet electrolyte to suppress lithium dendrite growth. *Chem Eng J* 2021;411:128508. DOI

38.　Zheng C, Lu Y, Su J, et al. Grain boundary engineering enabled high-performance garnet-type electrolyte for lithium dendrite free lithium metal batteries. *Small Methods* 2022;6:e2200667. DOI

39.　Kataoka K, Akimoto J. Large single-crystal growth of tetragonal garnet-type $Li_7La_3Zr_2O_{12}$ by melting method. *Solid State Ionics* 2020;349:115312. DOI

40.　Kataoka K. Oxide single crystals with high lithium-ion conductivity as solid electrolytes for all-solid-state lithium secondary battery applications. *J Ceram Soc Japan* 2020;128:7-18. DOI

41.　Kudo H, Wu C, Ihle H. Mass-spectrometric study of the vaporization of Li_2O_s and thermochemistry of gaseous LiO, Li_2O, Li_3O, and Li_2O_2. *J Nucl Mater* 1978;78:380-9. DOI

42.　Li Y, Han JT, Wang CA, Xie H, Goodenough JB. Optimizing Li^+ conductivity in a garnet framework. *J Mater Chem* 2012;22:15357-61. DOI

43.　Larraz G, Orera A, Sanjuán ML. Cubic phases of garnet-type $Li_7La_3Zr_2O_{12}$: the role of hydration. *J Mater Chem A* 2013;1:11419-28. DOI

44.　Huang X, Song Z, Xiu T, Badding ME, Wen Z. Sintering, micro-structure and Li^+ conductivity of Li_7-La_3Zr_2-NbO_{12}/MgO (x = 0.2-0.7) Li-garnet composite ceramics. *Ceram Int* 2019;45:56-63. DOI

45.　Cai J, Polzin B, Fan L, et al. Stoichiometric irreversibility of aged garnet electrolytes. *Mater Today Energy* 2021;20:100669. DOI

46.　Liu C, Rui K, Shen C, Badding ME, Zhang G, Wen Z. Reversible ion exchange and structural stability of garnet-type Nb-doped $Li_7La_3Zr_2O_{12}$ in water for applications in lithium batteries. *J Power Sources* 2015;282:286-93. DOI

47.　Pfeiffer H, Bosch P. Thermal stability and high-temperature carbon dioxide sorption on hexa-lithium zirconate ($Li_6Zr_2O_7$). *Chem Mater* 2005;17:1704-10. DOI

48.　Baral AK, Narayanan S, Ramezanipour F, Thangadurai V. Evaluation of fundamental transport properties of Li-excess garnet-type $Li_{5+2x}La_3Ta_{2-x}Y_xO_{12}$ (x = 0.25, 0.5 and 0.75) electrolytes using AC impedance and dielectric spectroscopy. *Phys Chem Chem Phys* 2014;16:11356-65. DOI PubMed

49.　Samsinger RF, Letz M, Schuhmacher J, et al. Fast ion conduction of sintered glass-ceramic lithium ion conductors investigated by impedance spectroscopy and coaxial reflection technique. *J Electrochem Soc* 2020;167:140510. DOI

50.　Dion F, Lasia A. The use of regularization methods in the deconvolution of underlying distributions in electrochemical processes. *J Electroanal Chem* 1999;475:28-37. DOI

51.　Zhang Y, Chen Y, Yan M, Chen F. Reconstruction of relaxation time distribution from linear electrochemical impedance spectroscopy. *J Power Sources* 2015;283:464-77. DOI

52.　Cheng L, Crumlin EJ, Chen W, et al. The origin of high electrolyte-electrode interfacial resistances in lithium cells containing garnet type solid electrolytes. *Phys Chem Chem Phys* 2014;16:18294-300. DOI

53.　Jones JC, Rajendran S, Pilli A, et al. *In situ* x-ray photoelectron spectroscopy study of lithium carbonate removal from garnet-type solid-state electrolyte using ultra high vacuum techniques. *J Vac Sci Technol A* 2020;38:023201. DOI

54.　Han F, Zhu Y, He X, Mo Y, Wang C. Electrochemical stability of $Li_{10}GeP_2S_{12}$ and $Li_7La_3Zr_2O_{12}$ solid electrolytes. *Adv Energy Mater* 2016;6:1501590. DOI

55.　Yuan K, Jin X, Xu C, et al. Fabrication of dense and porous Li_2ZrO_3 nanofibers with electrospinning method. *Appl Phys A* 2018;124:403. DOI

56.　Huang Y, Chen J, Ni J, Zhou H, Zhang X. A modified ZrO_2-coating process to improve electrochemical performance of

Li(Ni$_{1/3}$Co$_{1/3}$Mn$_{1/3}$)O$_2$. *J Power Sources* 2009;188:538-45. DOI

57. Tenhaeff WE, Rangasamy E, Wang Y, et al. Resolving the grain boundary and lattice impedance of hot-pressed Li$_7$La$_3$Zr$_2$O$_{12}$ garnet electrolytes. *ChemElectroChem* 2014;1:375-8. DOI

58. Kim Y, Yoo A, Schmidt R, et al. Electrochemical stability of Li$_{6.5}$La$_3$Zr$_{1.5}$M$_{0.5}$O$_{12}$ (M = Nb or Ta) against Metallic Lithium. *Front Energy Res* 2016;4:20. DOI

59. Tang J, Niu Y, Zhou Y, et al. H$_3$PO$_4$-induced Nano-Li$_3$PO$_4$ pre-reduction layer to address instability between the Nb-Doped Li$_7$La$_3$Zr$_2$O$_{12}$ electrolyte and metallic Li anode. *ACS Appl Mater Interfaces* 2023;15:5345-56. DOI

60. Niu Y, Yu Z, Zhou Y, et al. Constructing stable Li-solid electrolyte interphase to achieve dendrites-free solid-state battery: a nano-interlayer/Li pre-reduction strategy. *Nano Res* 2022;15:7180-9. DOI